# Carrier concentration and lattice absorption in bulk and epitaxial silicon carbide determined using infrared ellipsometry

Thomas E. Tiwald and John A. Woollam
*Center for Microelectronic and Optical Materials Research and Department of Electrical Engineering, University of Nebraska, Lincoln, Nebraska 68588-0511*

Stefan Zollner, Jim Christiansen, R. B. Gregory, T. Wetteroth, and S. R. Wilson
*Motorola Semiconductor Products Sector, MD M360, 2200 West Broadway, Mesa, Arizona 85202*

Adrian R. Powell
*ATMI/Epitronics, 7 Commerce Drive, Danbury, Connecticut 06810-4169*
(Received 16 February 1999)

We have measured the dielectric function of bulk nitrogen-doped 4H and 6H SiC substrates from 700 to 4000 $cm^{-1}$ using Fourier-transform infrared spectroscopic ellipsometry. Photon absorption by transverse optical phonons produces a strong reststrahlen band between 797 and 1000 $cm^{-1}$ with the effects of phonon anisotropy being observed in the region of the longitudinal phonon energy (960 to 100 $cm^{-1}$). The shape of this band is influenced by plasma oscillations of free electrons, which we describe with a classical Drude equation. For the 6H-SiC samples, we modify the Drude equation to account for the strong effective mass anisotropy. Detailed numerical regression analysis yields the free-electron concentrations, which range from $7\times10^{17}$ to $10^{19}\,cm^{-3}$, in good agreement with electrical and secondary ion mass spectrometry measurements. Finally, we observe the Berreman effect near the longitudinal optical phonon energy in $n-/n+$ homoepitaxial 4H SiC and hydrogen implanted samples, and we are able to determine the thickness of these surface layers. [S0163-1829(99)00240-4]

## I. INTRODUCTION

In recent years, infrared spectroscopic ellipsometers (IR-SE's) have gained sufficient accuracy and precision to be applied to the quantitative determination of optical properties associated with free carriers and lattice vibrations in semiconductors and insulators.[1–4] The technique has been applied to a number of materials problems, including: the transverse-optic (TO) phonon absorption and doping concentration in *n*-type GaAs,[5] one- and two-phonon absorption in LiF,[6,7] graded carrier concentration profiles in implanted and epitaxial silicon,[8,9] and epitaxial and bulk-doping concentrations for $In_xGaAs_{1-x}Sb$ epilayers on GaSb.[10]

IR-SE has been applied to the study of strong phonon anisotropy in bulk $\alpha$-$SiO_2$ and $\alpha$-$Al_2O_3$ by Humlíček and Röseler.[11,12] Thompson *et al.*[13] measured calcite using generalized IR-SE. The anisotropic effects of thin polycrystalline BN films were studied by Franke *et al.*[14]

The origin of the Berreman peak and its effect on IR-SE spectra has been described in detail by Röseler.[1] Humlíček, Henn, and Cardona[5] observed the Berreman effect in IR-SE spectra of doped GaAs, which they attributed to a carrier-depleted surface layer caused by surface band bending. Humlíček has recently discussed the issue of electric field distributions and energy dissipation for the Berreman effect (specifically for thin LiF films on Ag and Si substrates).[6,7]

The infrared optical properties of silicon carbide have been studied since the late 1950s (e.g., see Refs. 15–17). More recently, Engelbrecht and Helbig[18] explored the effects of anisotropy on the infrared reflectivity in the reststrahlen band of 6H-SiC. Macmillan, Henry, and Janzén[19] determined the thickness of *n*-SiC layers on $n+$SiC using infrared reflectivity. In this paper, we employ IR-SE in the quantitative measurement of the complex dielectric response of nitrogen-doped 4H and 6H silicon carbide crystals in the midinfrared (700 to 4000 $cm^{-1}$) range. Since IR-SE is particularly sensitive to free-carrier absorption as well as phonon and effective mass anisotropy, we will focus on these effects.

## II. EXPERIMENTAL PROCEDURES

The sample set consists of five bulk 4H and two bulk 6H SiC wafers obtained commercially, as well as two homoepitaxial ($n-/n+$) samples and a hydrogen-implanted substrate (see Table I). Such wafers are readily available from suppliers, such as Cree Research and ATMI/Epitronics. One lightly doped (*n*-) epilayer was approximately 0.75 $\mu$m thick with an electron density of $10^{16}\,cm^{-3}$ grown on a heavily nitrogen-doped ($n+$,$10^{19}\,cm^{-3}$) 4H SiC substrate. The other *n*- epilayer was $\approx$3.5 $\mu$m thick and was grown on a substrate with $2\times10^{18}$-$cm^{-3}$ nitrogen doping. The final sample consisted of a $10^{19}$-$cm^{-3}$ nitrogen-doped 4H SiC substrate implanted with $10^{16}\,H^+\,cm^{-2}$ at 100 keV. All 4H and 6H substrates were miscut 8° and 3.5° off the {0001} plane toward ⟨1120⟩, respectively.

The 4-$\mu$m epilayer was subjected to secondary ion mass spectrometry (SIMS) analysis on a Cameca IMS 6F magnetic sector instrument equipped with a normal incidence electron gun (NEG) for charge neutralization. The analytical parameters for this analysis were 10 keV $Cs^+$ primary ions with a current of about 150 nA rastered over a 150 $\mu$m $\times$150 $\mu$m area. Negative secondary ions were detected for

 

TABLE I. Results from using Eq. (3) to fit experimental data. The ac mobility (at 30 THz) in the last column was calculated using $\mu = e\tau/m^* m_0$. Free-carrier concentration values determined by Hall, Hg-probe CV or SIMS are provided for comparison (NA: not available).

| Sample | Polytype | $n$(IR-SE) ($10^{18}$ cm$^{-3}$) | $n$ (CV or SIMS[i]) ($10^{18}$ cm$^{-3}$) | Epi thickness ($\mu$m) nominal/IR-SE | $\tau$(fs) | $\varepsilon_{\infty\perp}$ | $\varepsilon_{\infty\parallel}$ | $\omega_{\mathrm{TO}\perp}$ (cm$^{-1}$)[c] | $\omega_{\mathrm{TO}\parallel}$ (cm$^{-1}$)[c] | $\omega_{\mathrm{LO}\perp}$ (cm$^{-1}$) | $\omega_{\mathrm{LO}\parallel}$ (cm$^{-1}$) | $\Gamma$ (cm$^{-1}$) | $\mu_\parallel/\mu_\perp$ (cm$^2$/Vs) |
|---|---|---|---|---|---|---|---|---|---|---|---|---|---|
| 1 | 4H | 2.8 | N/A | | 5.4 | 6.36 | 6.9 | 797 | 782 | 971 | 965 | 2.8 | 31/23 |
| 2 | 4H | 8.5 | 11 | | 5.9 | 6.5 | 7.7 | 797 | 782 | 971 | 965 | 2.8 | 33/25 |
| 3 | 4H | 9.2 | 6.1 | | 6.1 | 6.6 | 8.0 | 797 | 782 | 971 | 965 | 2.8 | 35/26 |
| 4 | 4H | 9.0 | 11 | | 5.8 | 6.4 | 7.7 | 797 | 782 | 971 | 965 | 2.8 | 33/24 |
| 5 | 4H | 8.0 | NA | | 6.3 | 6.2 | 7.7 | 797 | 782 | 971 | 965 | 2.8 | 36/26 |
| 6 | 6H | 0.66 | NA | | 3.9 | 6.3 | 7.0 | 797 | 788 | 972 | 970 | 4.7 | 4.0/27 |
| 7 | 6H | 0.2[d] | NA | | 3[c] | 6.6 | 6.8 | 797 | 788 | 972 | 967 | 2.7 | 3.1/21 |
| 8 ($n-/n+$) epi / | 4H | 0[c] | NA | 1/0.75 | | 6.6 | 6.9 | 797 | 782 | 974 | 973 | 4.5 | |
| substrate | | 10 | 10 | | 4.7 | 6.6[b] | 6.9[b] | 797 | 782 | 974[b] | 973[b] | 8.6 | 27/33 |
| 9 ($n-/n+$) epi / | 4H | 0[c] | 0.2[a] | 4/3.439 | | 6.6 | 6.9 | 797 | 782 | 970 | 964 | 1.4 | |
| substrate | | 2.0[d] | 2[a] | | 4.3 | 6.6[b] | 6.9[b] | 797 | 782 | 970[b] | 964[b] | 1.4[b] | 24/18 |
| 10 H-implant / | 4H | 0[c] | NA | NA/0.77 | | 6.6 | 7.8 | 797 | 782 | 973 | 968 | 12 | |
| substrate | | 7.0 | 11 | | 6.7 | 6.2 | 7.8 | 797 | 782 | 973[b] | 968[b] | 12[b] | 38/28 |

[a]Data from SIMS.

[b]Top layer and substrate values forced to be equal.

[c]Value fixed during fit.

[d]Carrier concentration N correlates with mean scattering time $\tau$.

$^{14}N^{13}C^-$ with a mass-resolving power of about 4000 to avoid mass interferences. The NEG was also used to avoid charging effects in the lighter doped epi region. The data was calibrated for concentration by analyzing a $^{14}N$ ion implanted SiC substrate (with a nitrogen dose of $10^{14}\,cm^{-2}$ at 100 keV) under the same conditions and applying the appropriate relative sensitivity factor to the unknown sample.

The infrared variable angle spectroscopic ellipsometer is a rotating-compensator instrument described elsewhere.[8,9] For this study, the spectral range was 700 to 4000 $cm^{-1}$ (2.5 to 14.3 $\mu$m, 0.089 to 0.496 eV) at a resolution of 16 $cm^{-1}$, with some measurements acquired at 4 and 1 $cm^{-1}$ resolutions. The beam is 8-mm wide at the sample, with a 3° angular spread. Data were taken at angles of incidence of 60°, 65°, and 70°, which yielded ellipsometric spectra with reasonable sensitivity and signal-to-noise ratios.

Reflection ellipsometry measures the change of the polarization state of light upon reflection from a sample surface, which is expressed as the ratio of the complex Fresnel reflection coefficients $r_p$ and $r_s$ (for light polarized parallel and perpendicular to the plane of incidence, respectively) (Ref. 20)

$$\rho=\frac{r_p}{r_s}=\tan(\Psi)e^{i\Delta}. \tag{1}$$

Specifically, $\tan(\Psi)$ is the ratio of the magnitudes of $r_p$ and $r_s$, and $\Delta$ is the phase difference between the coefficients.

The most comprehensive approach to measuring and analyzing hexagonal SiC, which has uniaxial anisotropy, would be generalized ellipsometry (e.g., see Azzam and Bashara,[18] or Schubert[21]). However, if we assume that the optic axis is perpendicular to the sample surface, there will be no cross conversion between *p*- and *s*-polarized light. This greatly simplifies the calculation of the Fresnel reflection coefficients, which, for an air ambient, become[20]

$$r_p=\frac{n_o n_e\cos\varphi-(n_e^2-\sin^2\varphi)^{1/2}}{n_o n_e\cos\varphi+(n_e^2-\sin^2\varphi)^{1/2}} \tag{2a}$$

and

$$r_s=\frac{\cos\varphi-(n_o^2-\sin^2\varphi)^{1/2}}{\cos\varphi+(n_o^2-\sin^2\varphi)^{1/2}}, \tag{2b}$$

where $n_o$ is the ordinary refractive index and $n_e$ is the extraordinary refractive index of the bulk, with $n_o=\sqrt{\varepsilon_o}$ and $n_e=\sqrt{\varepsilon_e}$. $\varphi$ is the angle of incidence. The assumption that the optic axis is perpendicular to the sample surface is not entirely correct—as we mentioned above, the 4H and 6H substrates are miscut by a few degrees. However, the miscuts are small enough that this assumption produces a reasonable first-order model for the data.

### III. EXPERIMENTAL RESULTS

The ellipsometric spectra, $\Psi$ and $\Delta$, for samples 1 and 2 (both 4H bulk samples but with different free carrier densities, see Table I) at $\varphi=65°$ are shown in Fig. 1. The spectra contain four readily observable features: the first being a strong reststrahlen band extending from 797 to 1000 $cm^{-1}$;

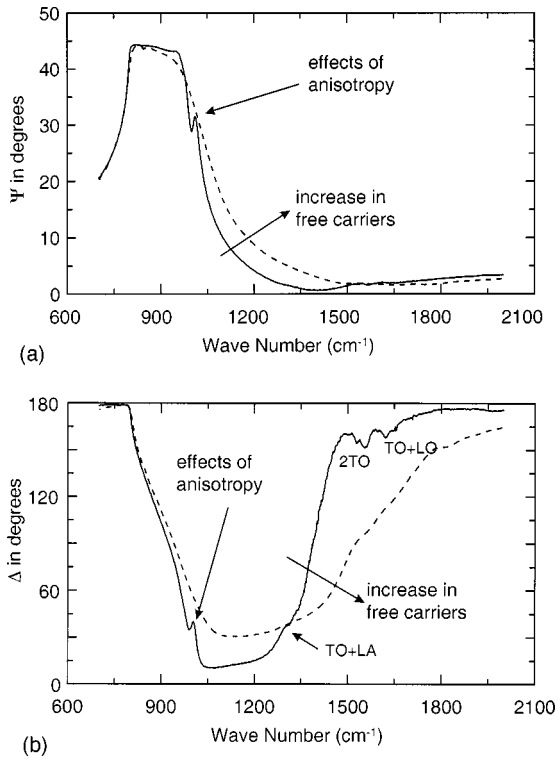


FIG. 1. Ellipsometric spectra $\Psi$ [Fig. 1(a)] and $\Delta$ [Fig. 1(b)] at $\varphi=65°$ for two 4H SiC substrate: Sample 1 (solid lines, $N\approx 3\times10^{18}\,cm^{-3}$) and Sample 2 (dashed lines, $N\approx 9\times10^{18}\,cm^{-3}$). The major effects of anisotropy, free carriers, and two-phonon summation bands are indicated.

the second, a group of two-phonon absorptions between 1300 and 1600 $cm^{-1}$; and the third, a sharp resonancelike structure around 1000 $cm^{-1}$ related to uniaxial anisotropy. Fourth, a comparison of data from the two samples reveals that an increase in free carriers tends to broaden and smooth the other spectral features.

These effects are also present in the pseudodielectric function, $\langle\varepsilon\rangle=\langle\varepsilon_1\rangle+i\langle\varepsilon_2\rangle$, which is calculated directly from the ellipsometric data from the same samples.[20] From Figs. 2(a) and 2(b) we observe that the midinfrared optical response of silicon carbide is dominated by the one-phonon lattice absorption at 797 $cm^{-1}$. However, the details seen in Fig. 2(b) demonstrate that there are additional contributions from free carriers (which cause a spectrum-wide dispersion in $\langle\varepsilon_1\rangle$ and $\langle\varepsilon_2\rangle$), phonon anisotropy (which causes the peak in $\langle\varepsilon_2\rangle$ at 1000 $cm^{-1}$), and the two-phonon summation bands[22] between 1300–1600 $cm^{-1}$. It is notable that these small contributions to the pseudodielectric function, which are two orders of magnitude smaller than the main phonon absorption at 797 $cm^{-1}$, have a strong effect on $\Psi$ and $\Delta$ in Fig. 1(b).

Figure 3 shows the ellipsometric spectra for samples 8 and 10, which are two heavily doped substrates (0.7 and $1.0\times10^{19}$ nitrogen $cm^{-3}$, respectively) that have been surface modified. Sample 8 has an undoped homoepitaxial layer, while sample 10 has been implanted with $10^{16}$ $H^+\,cm^{-2}$. The broad oscillations from 1500 to 4000 $cm^{-1}$ are interference effects caused by the contrast in refractive indices between the substrate and surface layers. Interference oscillations are also seen in the spectra for sample 9 (Fig. 4),

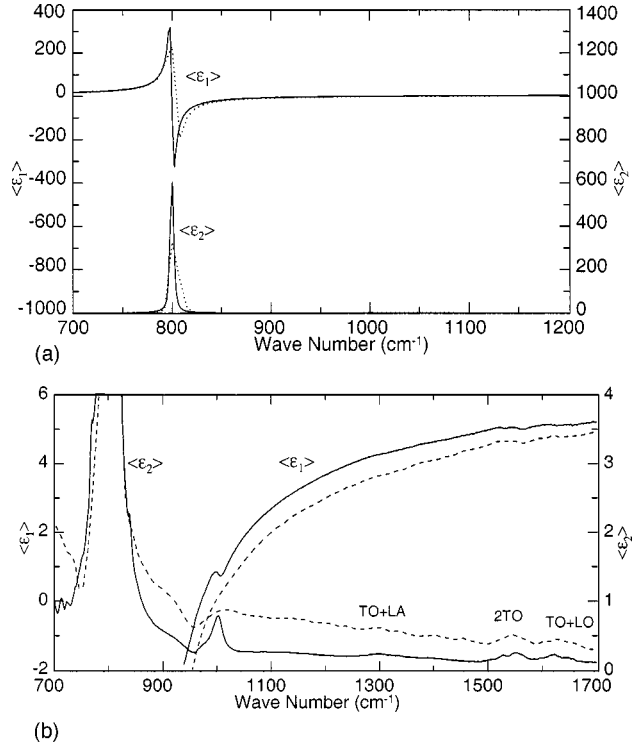


FIG. 2. Real and imaginary parts of the pseudodielectric function for SiC bulk ellipsometric data for samples 1($N \approx 3 \times 10^{18}$ cm$^{-3}$) and 2($N \approx 9 \times 10^{18}$ cm$^{-3}$). (a): The spectrum is dominated by the strong lattice absorption at 800 cm$^{-1}$. (b): Same as (a), but with a greatly reduced scale. The free carrier effects, two-phonon summation bands (1300–1600 cm$^{-1}$) and anisotropy-induced structure at 1000 cm$^{-1}$ can be seen. The two-phonon absorptions are marked.

which is an $\approx$3.5-$\mu$m homoepitaxial layer on a $2 \times 10^{18}$-cm$^{-3}$ nitrogen-doped substrate. The reststrahlen band of sample 9 is considerably different from those of samples 8 and 10, particularly in the region from $\omega_{LO\parallel,\perp}$ and above (see Fig. 5). The minima appearing near 975 cm$^{-1}$ in data for samples 8 and 10 are a result of the Berreman effect.[23] Sample 9 exhibits pair of shall minima around 970 cm$^{-1}$ and a deep minimum at 995 cm$^{-1}$. In Sec. VI, we shall demonstrate how sample 9's thick epilayer and low-substrate doping suppresses the Berreman effect and enhances the effects related to anisotropy.

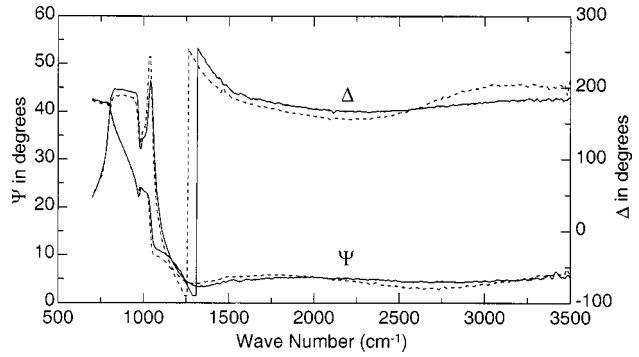


FIG. 3. Ellipsometric spectra ($\Psi$ and $\Delta$, $\varphi = 65°$) for sample 8, a 4H $n-/n+$ SiC homostructure (solid lines); and sample 10, a hydrogen-implanted 4H substrate (dashed lines).

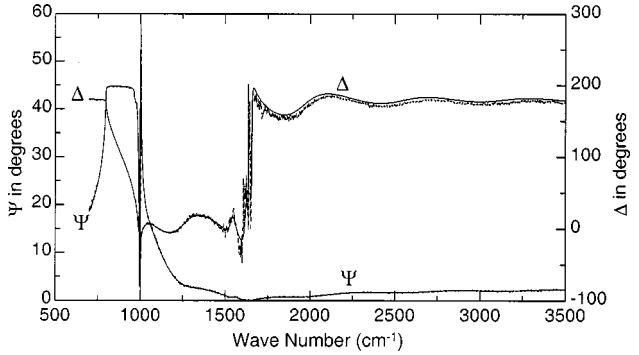


FIG. 4. Ellipsometric spectra ($\Psi$ and $\Delta$, $\varphi = 68°$) for sample 9, 4H 3.5 $\mu$m-thick $n-/n+$ homostructure (solid lines) and along with model results.

It is clear that IR-SE is sensitive to doping, phonon anisotropy, two-phonon summation bands, and surface layers (via the Berreman effect and interference oscillations). These effects are discussed in detail in the following sections.

## IV. SIC OPTICAL RESPONSE MODEL

Figures 2(a) and 2(b) show that the midinfrared optical response of silicon carbide is dominated by the one-phonon lattice absorption centered around 800 cm$^{-1}$ with additional contributions from free carrier and two-phonon summation bands, as well as residuals of the interband transitions. We model the uniaxially anisotropic contributions by combining a Lorentz oscillator for the one-phonon absorption with the Drude equation.[24,25] To this model, we add the weaker two-phonon summation bands, resulting in

$$\varepsilon = \begin{bmatrix} \varepsilon_x & 0 & 0 \\ 0 & \varepsilon_y & 0 \\ 0 & 0 & \varepsilon_z \end{bmatrix} = \begin{bmatrix} \varepsilon_\perp & 0 & 0 \\ 0 & \varepsilon_\perp & 0 \\ 0 & 0 & \varepsilon_\parallel \end{bmatrix}, \tag{3a}$$

where

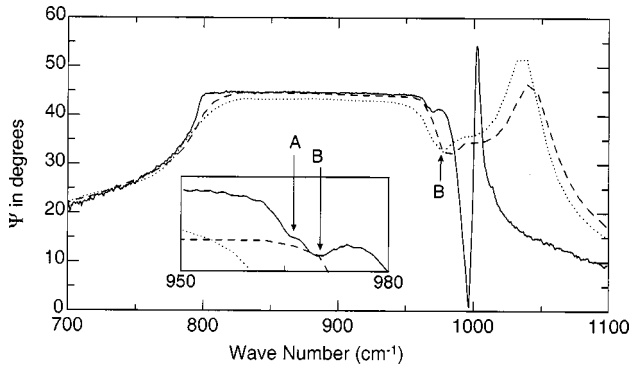


FIG. 5. Ellipsometric $\Psi$ spectra ($\varphi = 65°$) for the surface modified 4H-SiC samples 8 (dashed line), 9 (solid line), and 10 (dotted line) showing the reststrahlen region. Absorptions due to LO phonon anisotropy ($A$) and the Berreman effect ($B$) are marked. The inset details the LO phonon region of sample 9, which exhibits both absorptions.

$$\varepsilon_{\parallel,\perp}=\varepsilon_{\infty\parallel,\perp}+\frac{\varepsilon_{\infty\parallel,\perp}(\omega^2_{LO\parallel,\perp}-\omega^2_{TO\parallel,\perp})}{\omega^2_{TO\parallel,\perp}-\omega^2-i\omega\Gamma_{\parallel,\perp}}-\frac{4\pi Ne^2}{m^*_{\parallel,\perp}m_o}\frac{1}{\omega^2+i\omega\gamma}+\sum_{j=1}^{3}\frac{4\pi\rho_j\omega_j^2}{\omega_j^2-\omega^2-i\omega\gamma_j'}. \quad (3b)$$

For these samples, the quantity $\varepsilon_{\parallel}$ describes the dielectric response to electric fields polarized parallel to the surface normal (parallel to both the *z* axis of our coordinate system and the *c* axis of the crystal), and $\varepsilon_{\perp}$ describes the response to fields polarized parallel to the surface. In terms of the ordinary and extraordinary refractive indices described in Eq. (2), $\varepsilon_{\parallel}=\varepsilon_e=n_e^2$ and $\varepsilon_{\perp}=\varepsilon_o=n_o^2$. The value $\varepsilon_{\infty\parallel,\perp}$ represents the residual effects of the interband transitions parallel and perpendicular to the *c* axis. The second term in Eq. (3b) accounts for strong single-phonon lattice absorption, where $\omega_{TO\parallel,\perp}$ and $\omega_{LO\parallel,\perp}$ are the transverse and longitudinal optic phonon frequencies, respectively; and $\Gamma_{\parallel,\perp}$ are the phonon damping constants.

The third term is the classical Drude equation for free carriers. The plasma frequency is defined as $\omega_p^2=4\pi Ne^2/\varepsilon_{\infty\parallel,\perp}m^*_{\parallel,\perp}m_o$, where $N$ is the free carrier density, $e$ is the electron charge, and $m^*_{\parallel,\perp}m_o$ is the (anisotropic) effective mass. The parameter $\gamma=1/\tau$ is the free-carrier damping rate at the frequency $\omega$, and is assumed to be isotropic to reduce the number of free parameters to be determined.

We model the three largest of the weak two-phonon summation bands (see Figs. 1 and 2) with Lorentz oscillators. Because reflection spectroscopies such as ellipsometry are not likely to be sensitive to the anisotropic character of these weak absorptions, we represent them as isotropic oscillators in order to simplify the model.

Bechstedt *et al.*[26] provides a brief list, drawn from the literature, of values for $\varepsilon_{\infty\parallel}$ and $\varepsilon_{\infty\perp}$. For 4H-SiC, $6.78\leqslant\varepsilon_{\infty\parallel}\leqslant7.61$ and $6.56\leqslant\varepsilon_{\infty\perp}\leqslant7.54$ (averages: $\varepsilon_{\infty\parallel}=7.19$, $\varepsilon_{\infty\perp}=7.00$). For 6H-SiC, $6.68\leqslant\varepsilon_{\infty\parallel}\leqslant7.491$ and $\varepsilon_{\infty\perp}$ and $6.52\leqslant\varepsilon_{\infty\perp}\leqslant7.33$ (average: $\varepsilon_{\infty\parallel}=7.16$, $\varepsilon_{\infty\perp}=7.01$). In all cases, $\varepsilon_{\infty\parallel}$ is greater than $\varepsilon_{\infty\perp}$, by an average of 0.16. Similar results are seen in this study (see Table I).

For hexagonal SiC, the single lattice absorption described by the second term in Eq. (3b) represents a simplification of the one-phonon contributions to the mid-IR optical response. There are several complications because of the large number of atoms per unit cell (8 atoms per cell, 21 optical phonon modes for 4H SiC). Not only are there ''strong'' LO and TO modes, but also ''weak'' modes due to zone folding.[27] In 4H-SiC, we expect ''weak'' IR active modes at 838 $\text{cm}^{-1}$ ($A_1$), 610 $\text{cm}^{-1}$ ($A_1$), and 266 $\text{cm}^{-1}$ ($E_1$). (The Raman peaks observed near 776, 204, and 196 $\text{cm}^{-1}$ have $E_2$ symmetry and are IR inactive.) Because these zone-folding-related peaks are either weak, IR forbidden, or out of our spectral range, we expect them to have little influence on the spectra measured here.

For our analysis, we ignore all but the strong IR-active phonon modes. These have been previously measured.[14,25] For 6H SiC, modes parallel to the *c* axis (extraordinary optical response) are $\omega_{\text{TO}\parallel}=788\,\text{cm}^{-1}$ and $\omega_{\text{LO}\parallel}=964\,\text{cm}^{-1}$, modes perpendicular to the *c* axis (ordinary optical response) are $\omega_{\text{TO}\perp}=797\,\text{cm}^{-1}$ and $\omega_{\text{LO}\perp}=970\,\text{cm}^{-1}$. For 4H-SiC, we will use $\omega_{\text{TO}\parallel}=782\,\text{cm}^{-1}$ and $\omega_{\text{TO}\perp}=797\,\text{cm}^{-1}$ from Feldman *et al.*[27] (they found the LO modes to be $\omega_{\text{LO}\parallel}=\omega_{\text{LO}\perp}=970\,\text{cm}^{-1}$ within experimental uncertainty).

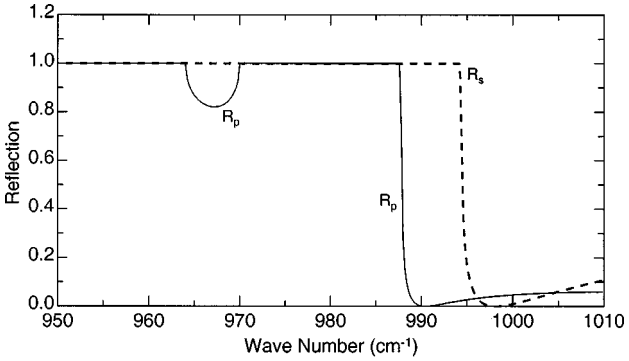


FIG. 6. Polarized reflectivity spectra, $\varphi=70°$, $R_p$ (solid line) and $R_s$ (dashed line), for a 6H SiC uniaxial bulk model without phonon damping or free carriers.

### A. Effects of anisotropy

Uniaxial anisotropy strongly influences the ellipsometric spectra in the region between $\varepsilon_{\parallel,\perp}=0$ (i.e., $\omega_{\text{LO}\parallel,\perp}$) and $\varepsilon_{\parallel,\perp}=1$. To illustrate this, we examine the *p*- and *s*-plane reflectivities, $R_p=|r_pr_p^*|$ and $R_s=|r_sr_s^*|$, keeping in mind that ellipsometry measures the complex ratio $r_p/r_s$. From Eqs. (2a) and (2b), we can calculate $R_p$ and $R_s$ for a 6H SiC uniaxial substrate model (*c* axis oriented normal to surface) using the transverse and longitudinal optic phonon values listed in previous section, with no phonon damping or free carrier absorption ($\Gamma_{\parallel,\perp}=0$ and $N=\omega_p=0$). The resulting spectra are shown in Fig. 6. $R_s$ is dominated by a single band of total external reflection, while $R_p$ is split into two bands of total reflection separated by a partially reflecting region between $\omega_{\text{LO}\perp}$ and $\omega_{\text{LO}\parallel}$.

This split in total reflection for $R_p$ is a manifestation of birefringence. It arises from Snell's law when the optic axis is orientated normal to the surface, and can be stated in the following form:[16,28,29]

$$\varepsilon_1\cdot\sin^2\varphi=\varepsilon_{\perp}\cdot\sin^2\varphi_s=\frac{\varepsilon_{\perp}\varepsilon_{\parallel}\cdot\sin^2\varphi_p}{\varepsilon_{\perp}\cdot\sin^2\varphi_p+\varepsilon_{\parallel}\cdot\cos^2\varphi_p}. \quad (4)$$

From this equation, we can calculate $\varphi_s$ and $\varphi_p$, the angles of refraction for *s*- and *p*-polarized wave vectors for a known angle of incidence $\varphi$. Assuming $\varepsilon_1=1$ for air

$$\sin\varphi_s=\frac{\sin\varphi}{\sqrt{\varepsilon_{\perp}}} \quad (5)$$

and

$$\sin\varphi_p=\frac{\sin\varphi}{\sqrt{\sin^2\varphi\left(1-\frac{\varepsilon_{\perp}}{\varepsilon_{\parallel}}\right)+\varepsilon_{\perp}}}. \quad (6)$$

Defining the square of the denominator of Eq. (6) as an effective dielectric constant and assuming $\varepsilon_1=1$, Eq. (4) can be rewritten as

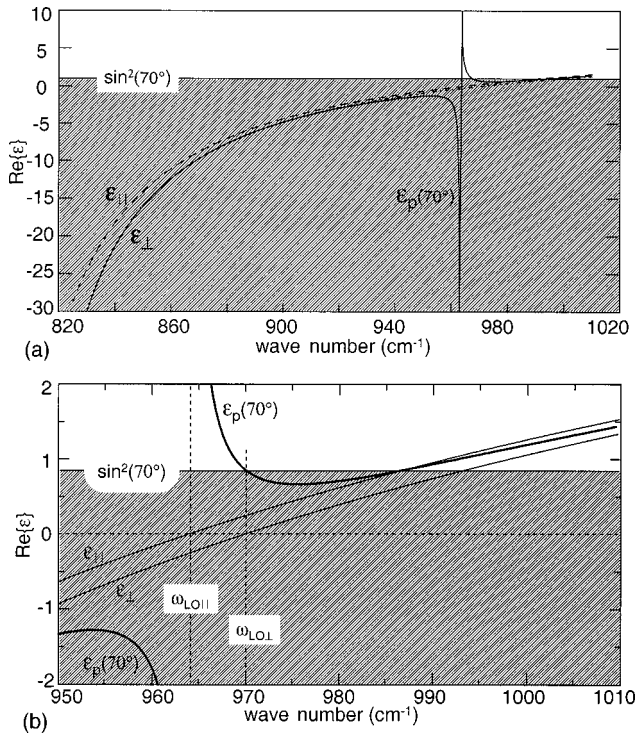


FIG. 7. (a) Dielectric constants $\varepsilon_\perp$, $\varepsilon_\parallel$, and $\varepsilon_p$ ($\varphi = 70°$) for a 6H SiC uniaxial bulk model without phonon damping or free carriers. $\varepsilon_p$ has a pole at $\omega_{LO\parallel}$ (964 $cm^{-1}$). (b) $\varepsilon_\perp$, $\varepsilon_\parallel$, and $\varepsilon_p$ in the region around $\omega_{LO\parallel}$ and $\omega_{LO\perp}$. Total external reflection occurs whenever $\epsilon_\parallel$ and $\epsilon_p$ fall below $\sin^2(70°)$.

$$\sin^2\varphi = \varepsilon_\perp \cdot \sin^2\sigma_s = \varepsilon_p \cdot \sin^2\varphi_p, \tag{7a}$$

where

$$\varepsilon_p = \sin^2\varphi\left(1 - \frac{\varepsilon_\perp}{\varepsilon_\parallel}\right) + \varepsilon_\perp. \tag{7b}$$

The dielectric constant $\varepsilon_p$ is the response of the uniaxial material to *p*-polarized light whose wave vector is refracted at an angle $\varphi_p$ with respect to the optic axis (surface normal). Figures 7(a) and 7(b) graph $\varepsilon_p$ from the same 6H-SiC uniaxial substrate model used to simulate $R_p$ and $R_s$ in Figs. 6(a) and 6(b). Note that $\varepsilon_p$ has a pole at $\omega = \omega_{LO\parallel}$.

In anisotropic materials, the wave vector direction for *p*-polarized light is, in general, different from the energy flow direction or ray vector.[30] That is, $\varphi_p$ generally does not equal the ray vector angle, which we will call $\varphi_p'$. This is true even under the condition of total external reflection,[31,32] when the energy of the incident light is neither absorbed nor propagated into a material (i.e., the ray or time-averaged Poynting vector is not directed into the material). Because of this, we must be careful how we calculate the critical angle $\varphi_c$, the angle of incidence that defines onset of total external reflection. Fortunately, when the optic axis of a material is normal to the surface, the ray vector for *p*-polarized light coincides with the wave vector under conditions of total external reflection[26,29,30]—that is, $\varphi_p' = \varphi_p = \pi/2$. This means we can still define the critical incident angle for total reflection as the angle at which the refracted wave vector begins to run parallel to the surface; that is, in Eq. (7a), where $\varphi_p = \pi/2$. Thus, the condition of total external reflection exists when $\sin^2\varphi_p \geq 1$, or from Eq. (7a)

$$\varepsilon_p \leq \sin^2\varphi. \tag{8}$$

For *s*-polarized light, the Poynting vector is parallel to the wave vector at all times. Therefore, total external reflection of *s*-polarized light occurs when $\sin^2\varphi_s \geq 1$; or from Eq. (5), when

$$\varepsilon_\perp \leq \sin^2\varphi. \tag{9}$$

The spectral regions where total external reflection exists can be determined graphically by plotting $\sin^2\varphi$, $\varepsilon_p$, and $\varepsilon_\perp$ together, as has been done in Figs. 7(a) and 7(b). The shaded area, where $\varepsilon_p$ or $\varepsilon_\perp$ is less than $\sin^2\varphi$, is the region of total external reflection. Note that the pole at $\varepsilon_p = \omega_{LO\parallel}$ creates a split in the *p*-polarized reststrahlen band.

If we substitute Eq. (7b) into Eq. (8), we can specify the conditions of total reflection for the various conditions of positive and negative $\varepsilon_\perp$ and $\varepsilon_\parallel$. For 4H- and 6H-SiC, where $\omega_{TO\parallel} < \omega_{TO\perp} < \omega_{LO\parallel} < \omega_{LO\perp}$, the results are given in Table II.

These results are combined in Fig. 8 (for the same undoped, undamped model), which shows the regions of total external reflection as a function of wave number and angle of incidence. In the neighborhood of the TO phonon, total reflection starts at $\omega = \omega_{TO\perp}$ independent of the angle of incidence. This is because the extremely large refractive index in this spectral region always refracts the light at nearly normal to the surface, regardless of the incident angle, causing to interact only with the *c*-axis TO phonon modes. The reststrahlen band splits at $\omega_{LO\parallel}$, with the lower band bounded by

TABLE II. Conditions for Total External Reflection of *p*-polarized light.

| Conditions of $\varepsilon_\perp$ and $\varepsilon_\parallel$ | Total External Reflections occurs: |
|---|---|
| $\varepsilon_\perp$ and $\varepsilon_\parallel$ both $<0$ ($\omega_{TO\perp} < \omega < \omega_{LO\parallel}$) | For all values |
| $\varepsilon_\perp$ and $\varepsilon_\parallel$ both $>0$ ($\omega < \omega_{TO\parallel}, \omega > \omega_{LO\perp}$) | When $\varepsilon_\parallel < \sin^2\varphi$. |
| $\varepsilon_\parallel > 0$ and $\varepsilon_\perp < 0$ ($\omega_{LO\perp} < \omega < \omega_{LO\parallel}$) | When $\varepsilon_\parallel > \sin^2\varphi$ |
| $\varepsilon_\perp > 0$ and $\varepsilon_\parallel < 0$ ($\omega_{TO\parallel} < \omega < \omega_{TO\perp}$) | Never |

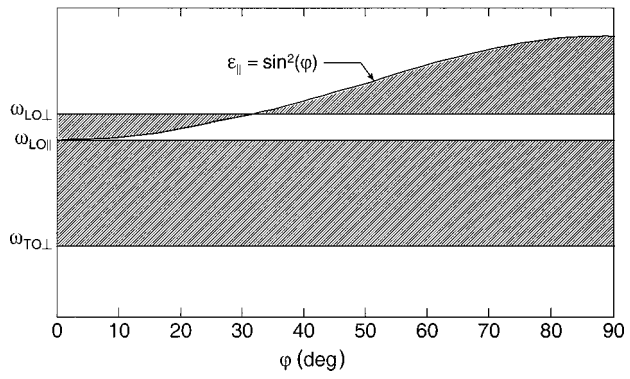


FIG. 8. Frequency regions of total external reflection (hatched area) angle of incidence $\varphi$ for any surface normal uniaxial material where $\omega_{TO\parallel} < \omega_{TO\perp} \omega_{LO\parallel} < \omega_{LO\perp}$, such as is the case for 4H- and 6H-SiC.

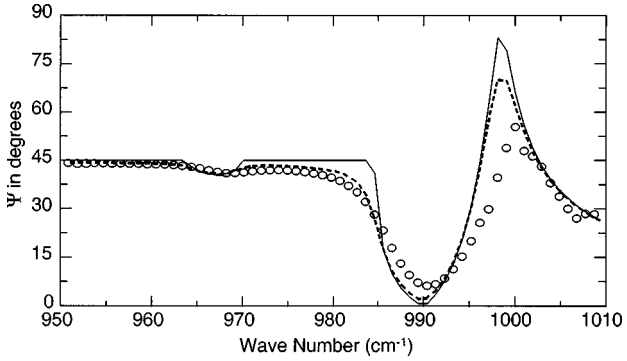


FIG. 9. The ellipsometric $\Psi$ spectra for Sample 6 (circles), a lightly doped 6H-SiC substrate, as well as the uniaxial bulk model without damping (solid line) and with damping of $\Gamma = 2\ \mathrm{cm}^{-1}$ (dashed line).

the region from $\omega_{\mathrm{TO}\perp} < \omega < \omega_{\mathrm{LO}\parallel}$ and the upper band bounded by $\omega_{\mathrm{LO}\perp}$ and $\varepsilon_{\parallel} = \sin^2\varphi$. The two bands merge into a single band only at $\varphi = 0°$.

In Fig. 9, the ellipsometric $\Psi$ spectrum is generated from the same model (solid line). Even without damping or free carrier effects, the model qualitatively reproduces the spectra of Sample 6, a bulk 6H SiC substrate. A minimum in $\Psi$ and $R_p$ occurs at $\varepsilon_{\parallel} = \varepsilon_p = 1$, a maximum in $\Psi$ occurs at $\varepsilon_{\perp} = 1$ where $R_s$ is at a minimum. By adding a reasonable amount of damping to the phonon dispersion—i.e., setting $\Gamma_{\parallel} = \Gamma_{\perp} = 2\ \mathrm{cm}^{-1}$, dashed line—we can begin to match the line shapes found in the data.

### B. Effects of free carriers

The addition of free carriers produces an additional dispersion throughout the spectral range in accordance with Eq. (3b), with increasing effect at longer wavelengths. In the region of $0 \leqslant \varepsilon_{\parallel,\perp} \leqslant 1$ the presence of free carriers strongly alters the line shape produced by phonon anisotropy. As Fig. 10 shows, an *isotropic* free carrier effect (dashed line)-that is, when $m_{\perp}^* = m_{\parallel}^*$ in Eq. (3b)—tends to dampen the anisotropic effects at higher carrier levels. When $m_{\perp}^*$ is sufficiently different from $m_{\parallel}^*$, the spectrum retains its anisotropic nature even at high-carrier concentrations (solid line), although the line shapes are considerably altered.

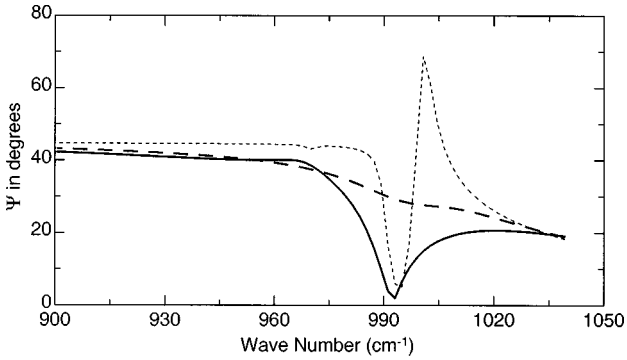


FIG. 10. Comparison of $\Psi$ for isotropic (dashed line, $m_{\perp}^* = m_{\parallel}^* = 0.47$) and anisotropic (solid line, $m_{\perp}^* = 0.25$, $m_{\parallel}^* = 1.7$) effective mass 6H-SiC models at $1.6 \times 10^{19}\ \mathrm{cm}^{-3}$ carrier concentrations. Dotted line is for no carriers. The damping is $\Gamma = 2\ \mathrm{cm}^{-1}$, with $\tau = 1$ fs and $\varphi = 65°$.

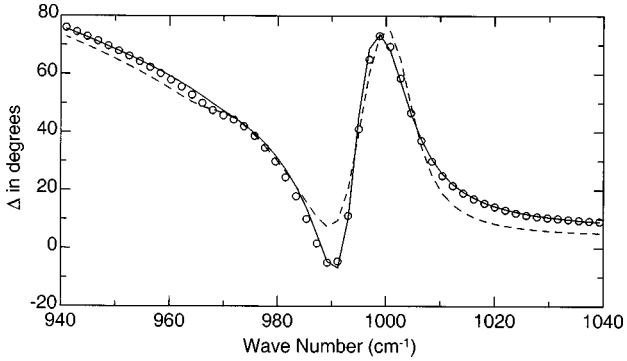


FIG. 11. Comparison for best fit models for isotropic (dashed line, $m_{\perp}^* = m_{\parallel}^* = 0.5$) and anisotropic (solid line, $m_{\perp}^* = 0.25$, $m_{\parallel}^* = 1.7$) effective mass for 6H-SiC sample 6. The circles are the experimental data at $\varphi = 65°$.

Both the 4H and 6H-SiC polytypes have nonisotropic conduction bands with several equivalent band minima.[33,34] For 6H-SiC, Yoshida[35] lists the axial effective mass $m_{\parallel}^* = 1.3$ (Hall effect), 1.5 (Faraday rotation), and 1.7 (IR reflection). Son *et al.*[36] measured $m_{\parallel}^* = 2.0$ for 6H-SiC using the technique of optically detected cyclotron resonance (ODCR). Devaty and Choyke[34] point out that $m_{\parallel}^*$ might depend significantly on the filling of a nonparabolic conduction band near the band minima, which implies that $m_{\parallel}^*$ depends on the doping density. The 6H-SiC planar effective mass, $m_{\perp}^*$, as measured by Faraday rotation, IR reflection, IR absorption, and IR birefringence,[35] ranges from 0.23 to 0.26.

For the more heavily doped 6H-SiC (sample 6), the fit was greatly improved if we used anisotropic effective mass values of $m_{\perp}^* = 0.25$ and $m_{\parallel}^* = 1.7$ instead of an isotropic value of $m^* = 0.5$ (see Fig. 11). The data for the more lightly doped 6H-SiC (sample 7) is not sensitive to effective mass anisotropy because of the low level of free-carrier absorption.

In contrast to the 6H-SiC polytype, the 4H-SiC effective mass tensor is more nearly isotropic. Yoshida[33] lists the 4H-SiC effective mass values as $0.19 \leqslant m_{\parallel} \leqslant 0.22$, and $0.18 \leqslant m_{\perp}^* \leqslant 0.24$. However, Lambrecht, Limpijumnong, and Segall[37] claim that these values are ''incorrect'' because of the ''use of an oversimplified model.'' They favor results from ODCR and from their own band-structure calculations, which yield values of $m_{\parallel}^* = 0.28$ and $m_{\perp}^* = 0.41$. Son *et al.*[38] measured $m_{\parallel}^* = 0.29$ and $m_{\perp}^* = 0.42$, using ODCR. For our data, the application of either an anisotropic or isotropic effective mass in the 4H-SiC model worked equally well, so we chose to fit those data with the simpler isotropic effective mass model, with $m_{\parallel}^* = m_{\perp}^* = 0.36$.

The free-carrier effects can clearly be seen in the pseudodielectric spectra in Fig. 2(b). The ellipsometric data are particularly sensitive to the free carrier density $N$, as well as $\omega_{\mathrm{LO}\parallel}$ and $\omega_{\mathrm{LO}\perp}$ (Fig. 1), because of the proximity of the incidence angle $\varphi$ to the pseudo-Brewster angle and zero crossing of $\mathrm{Re}(\varepsilon)$ at $\omega_{\mathrm{LO}}$. The three weak two-phonon summation bands are also included in the model because we found that without their subtle influence on spectral line shape in the 1200 to 1700 $\mathrm{cm}^{-1}$ range, the data fit results in a value for $N$ that is clearly inconsistent with the fit in the reststrahlen band. There is also considerable sensitivity to

free-carrier effects at the longer wavelengths (700–800 $cm^{-1}$) due to the $1/(\omega^2+i\omega\gamma)$ dependence of the Drude term.

The free-carrier damping rate $\gamma$ depends on the inverse of the mean scattering time, i.e., $\gamma=1/\tau$. However, the scattering time is frequency dependent; therefore, $\tau_{IR}$, which we measured at roughly 30 THz (1000 $cm^{-1}$) is not necessarily equal to $\tau_{DC}$, the scattering time found in dc or low-frequency measurements. The scattering time and effective mass are related to the infrared-frequency mobility through $\mu_{IR}=e\tau_{IR}/m^*m_0$.

The scattering time and the mobility also depend upon carrier concentration. According to Harris,[35] the dc mobility in 3C SiC depends on the electron concentration $N$ via $\mu_n(N)=4.82\times10^9\times N^{-0.424}$, where $\mu$ is in units of $cm^2/Vs$ and $N$ in $cm^{-3}$. Using the relation $\tau=m^*m_0\mu/e$ and assuming that $N=6\times10^{18}\,cm^{-3}$ and an average $m^*=0.36$ (for 4H SiC), we would expect a dc scattering time of about 11 fs. The IR scattering times calculated from our data are of the same order of magnitude.

For a typical SiC substrate carrier density of $10^{18}\,cm^{-3}$, the plasma frequency is about 200 $cm^{-1}$. For a scattering time $\tau$ of 10 fs, the scattering rate is 100 THz, which corresponds to $h\gamma/2\pi=531\,cm^{-1}$. Since the scattering rate is larger than the plasma frequency, the plasma oscillations are strongly overdamped. This—combined with the fact that our spectral range does not extend to the plasma edge—leads to parameter correlations between $\tau$ and $N/m^*$ in the numerical regression analysis, particularly for carrier concentrations in the low-$10^{18}\,cm^{-3}$ range and below.

## V. BULK SAMPLE ANALYSIS

We applied Eqs. (3a) and (3b) to our experimental data for bulk substrates (samples 1 to 7, see Table I) which we assumed to be infinitely thick (i.e., no backside reflections) and uniaxially anisotropic with the optic axis perpendicular to the sample surface. We then optimized the various parameters until the model fit the ellipsometric data using the procedure similar to Herzinger *et al.*[39]

The model shown in Eqs. (3a) and (3b) contains 21 parameters. For each polytype, we fixed $m_\perp^*$, $m_\parallel^*$, $\omega_{TO\parallel}$, and $\omega_{TO\perp}$ to the values found in the literature, as described in the previous section. To further reduce the number of parameters, we assumed $\Gamma_\parallel=\Gamma_\perp=\Gamma$. [We are already assuming that free-carrier damping factor $\gamma(=1/\tau)$ is isotropic.] We then determined the 16 remaining parameters by fitting them to data for each sample.

Normally, a numerical fitting procedure for such a large set of parameters would result in a number of correlations. Fortunately, many of the parameters affect different regions of the spectra. Convergence on a set of optimized, uncorrelated parameters can be accomplished by restricting the spectral region and floating only those parameters that apply to that region. For instance, the nine parameters for the weak two-phonon oscillators ($\rho_j$, $\omega_j$, and $\gamma_j'$, $j=1,2,3$) primarily affect only the wavelength regions from 1200 to 2000 $cm^{-1}$. The parameters $\omega_{TO\parallel}$, $\omega_{TO\perp}$, $\omega_{LO\parallel}$, $\omega_{LO\perp}$, $\Gamma$, $m_\parallel^*$, $m_\perp^*$, and $\gamma(=1/\tau)$ primarily affect the spectral region from 700 to 1200 $cm^{-1}$. Both spectral regions are affected by $\varepsilon_\parallel$, $\varepsilon_\perp$ and the carrier concentration $N$, so these three parameters would be floated for both spectral regions. We iteratively fit the appropriate parameters in the restricted spectral regions until it is evident that all the floated parameters are converging to a solution. Then all 16 parameters are floated at once, fitting across the entire spectral range.

TABLE III. Center Energies for two-phonon summation bands from this study and Ref. 18.

| Polytype | TO+LA ($cm^{-1}$) | 2TO ($cm^{-1}$) | TO+LO ($cm^{-1}$) |
|---|---|---|---|
| 4H (this study) | 1327±3 | 1547±1 | 1627±2 |
| 6H (this study) | 1302±2 | 1538±1 | 1630±2 |
| 6H & 15H (Ref. 18) | 1308 | 1548 | 1622 |

Table I shows the results of the fit to experimental data using Eq. (3) for all the samples. The nominal free carrier concentrations, when available (from Hall or Hg-probe CV measurements performed by the wafer suppliers, or from SIMS measurements), are provided for comparison. The mobility $\mu_{IR}$ was calculated using $\mu_{IR\parallel,\perp}=e\tau_{IR}/m_{\parallel,\perp}^*m_0$.

The optimized center energies for the two-phonon summation-band Lorentz oscillators, along with the center energies measured by Patrick and Choyke,[20] are provided in Table III. Note that there is reasonable agreement between the two studies, particularly considering that the line shapes of the summation bands are decidedly not Lorentzian (see Ref. 18).

The minimum detectable free electron concentration is approximately $10^{18}\,cm^{-3}$. The primary limiting factor is the maximum wavelength of 14 $\mu$m, which is considerably shorter than the plasma wavelengths for these samples (about 50 $\mu$m for carrier densities of $10^{18}\,cm^{-3}$). The result is correlation between the electron density and mean scattering time at lower concentrations. This is not a fundamental limitation, however. Recent improvements in commercial Fourier transform infrared ellipsometers or synchrotron beam lines[40] allow measurements to 50 $cm^{-1}$ (200 $\mu$m), which would significantly improve our technique's sensitivity free carriers in SiC or other semiconductors.

## VI. EPILAYER AND HYDROGEN IMPLANTED SAMPLES

Three surface-modified 4H-SiC samples were also measured, two homoepitaxial $n-/n+$ samples and a hydrogen-implanted sample described in Sec. II. The spectra from all three samples have broad, low-amplitude interference oscillations in the region from 1500 to 3500 $cm^{-1}$ (see Figs. 3 and 4). These are the result of contrast in the refractive index between the doped substrates and the surface layers, which have lower carrier concentrations. All three samples also have sharp structures between 960 and 1030 $cm^{-1}$ (see Fig. 5). The structures arise from a combination of the bulk 4H-SiC anisotropy mechanisms and the Berreman effect, which we now discuss.

Figures 12(a) and 12(b) show $R_p$ spectra generated from two different epilayer models that are identical ($N_{epi}=0$, $\tau=4$ fs, $\omega_{LO\parallel}=964\,cm^{-1}$, $\omega_{LO\perp}=970\,cm^{-1}$, $\Gamma=1.4\,cm^{-1}$)

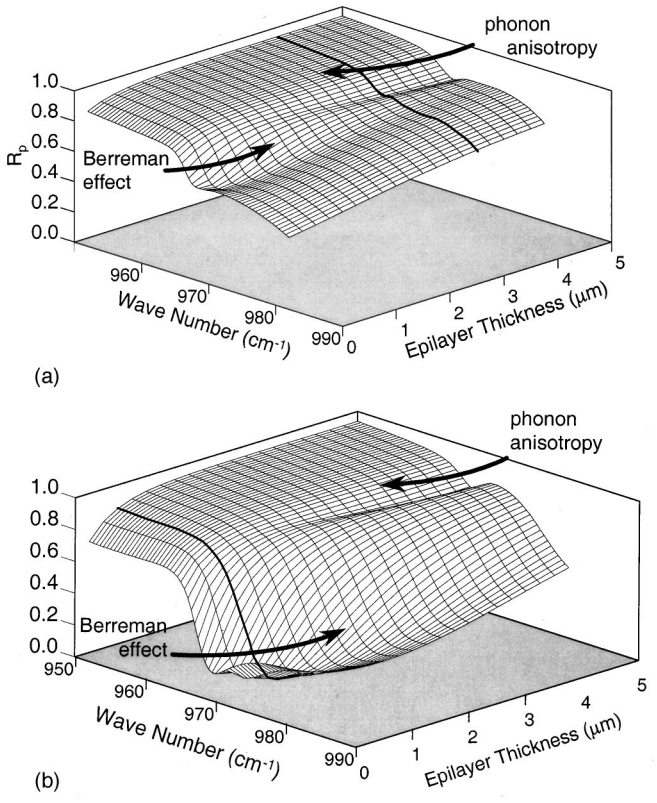


FIG. 12. Simulated $R_p$ ($\varphi = 65°$) plot for 4H-SiC epilayer models with epilayer thicknesses ranging from 0.25 to 5.0 $\mu$m. The models are identical except for the substrate doping: $2 \times 10^{18}\,\mathrm{cm}^{-3}$ for 12(a), and $1 \times 10^{19}\,\mathrm{cm}^{-3}$ for 12(b). The thinner epilayers include a minimum due to the Berreman effect, while thicker epilayers feature the same $\omega_{\parallel} - \omega_{\perp}$ minima found in bulk samples caused by phonon anisotropy. The dark line at the 3.5-$\mu$m cross section in 12(a) is the approximate $R_p$ spectrum for sample 9. A similar line at the 0.75-$\mu$m cross-section in 12(b) approximates $R_p$ for samples 8 and 10.

except for the substrate doping [$2 \times 10^{18}\,\mathrm{cm}^{-3}$ for Fig. 12(a) model and $1 \times 10^{19}\,\mathrm{cm}^{-3}$ for Fig. 12(b) model]. The epilayer thicknesses of both models are varied from 0.25 to 5 $\mu$m. In both figures, the dip in $R_p$ between $\omega_{\mathrm{LO}\parallel}$ and $\omega_{\mathrm{LO}\perp}$ (which is indicative of phonon anisotropy) becomes more pronounced as epilayer thickness increases. This is expected, since phonon damping limits the penetration depth of the light, causing thicker epilayers to behave like undoped, bulk 4H-SiC.

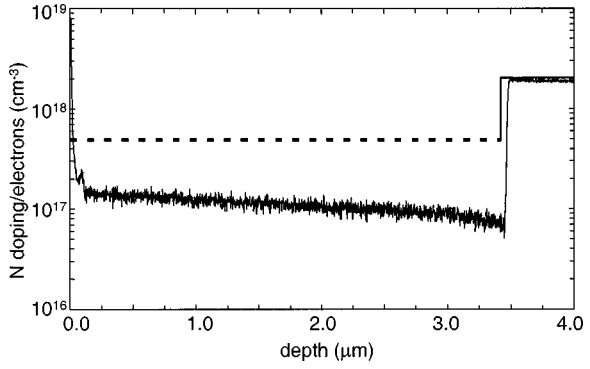


FIG. 13. Free-carrier concentration profile derived from IR-SE data, heavy solid line (heavy dotted line for region below IR-SE free-carrier detection limits) and SIMS nitrogen depth profile (light solid line) for sample 9.

Thinner epilayers are dominated by an absorption in $r_p$ called the Berreman effect,[1,5,21,41] which occurs at frequencies above epilayer's $\omega_{\mathrm{LO}\perp}$ and $\omega_{\mathrm{LO}\parallel}$ energies. Note that the effect is stronger for when substrate doping increases from $2 \times 10^{18}$ to $1 \times 10^{19}\,\mathrm{cm}^{-3}$ [compare minimum $R_p$ in Fig. 12(a) to Fig. 12(b)]. As doping increases, the substrate becomes more ''metal-like''—i.e., increased plasmon-phonon interactions cause the zero crossing of $\mathrm{Re}(\varepsilon_{\mathrm{substrate}})$ to shift to higher wave numbers—and the Berreman effect is enhanced.

The approximate $R_p$ spectrum for sample 9 is represented in Fig. 12(a) by the dark line on the surface plot along the 3.5-$\mu$m cross section. A similar line along the 0.75-$\mu$m cross section for samples 8 and 10 is shown in Fig. 12(b). Figure 5 shows the ellipsometric $\Psi$ spectra for the three samples in this region. Since the Berreman effect is *not* manifested in $r_s$, $\Psi$ is qualitatively similar to the $r_p$ cross sections of Figs. 12(a) and 12(b). Samples 8 and 10 have Berreman minima at about 980 $\mathrm{cm}^{-1}$ [Figs. 5 and 12(b)]. Both $r_p$ and $\Psi$ exhibit phonon anisotropy and the Berreman effect in sample 9, the 3.5-$\mu$m epilayer [see Fig. 12(a), also inset in Fig. 5].

We do not observe the Berreman effect in bulk SiC samples. In an earlier paper, three of us (S.Z., T.E.T, and J.A.W.) reported a peak in bulk SiC samples near the LO energy that we misinterpreted as a Berreman peak and attributed to surface depletion.[42] In fact, the observed structure is the result of phonon and free-carrier anisotropy, as described in the preceding section.

The data analysis of these surface-modified samples consists of optimizing a model for each sample that included an epilayer with the same phonon absorption as the substrate, but with a different carrier density. It became readily apparent during the fitting procedure that the free-carrier concentrations of the epilayers were below our detection limits. Therefore, we set $N = 0$ in the epilayer, then fit for epilayer thicknesses as well as $N$, $\tau$, $\varepsilon_{\infty\perp}$, and $\varepsilon_{\infty\parallel}$ in the substrates. In the epilayers, the parameters $\varepsilon_{\infty\perp}$ and $\varepsilon_{\infty\parallel}$ were forced to be the same as that of the substrates. The resulting fits were quite good (e.g., see sample 9 fit in Fig. 4).

The optimized models for samples 8 and 9 reproduce both the broad interference oscillations between 2000 and 4000 $\mathrm{cm}^{-1}$ as well as the sharp features found near the LO phonon frequencies around 1000 $\mathrm{cm}^{-1}$. The optimized ellipsometric model of sample 9 compares favorably to a SIMS nitrogen depth profile, as shown in Fig. 13. Although one might expect the chemical vapor deposition (CVD) epilayer growth process to produce a graded diffusion layer of nitrogen, a graded diffusion-layer model[9] does not significantly improve the fit. This indicates a minimum of nitrogen out diffusion during growth, which is supported by the abrupt interface seen in the SIMS profile.

The epilayer thickness of the IR-SE model free carrier profile is less than that indicated in the SIMS dopant profile (see Fig. 13). A similar shift in thickness was also seen in infrared reflectivity studies of Si epilayers by Harbecke, *et al.*[43] The appearance of the shift in two separate studies of different semiconductors suggests that the shift might be real, being the result of free carriers diffusing beyond the metallurgical interface of the dopant species. This shift is

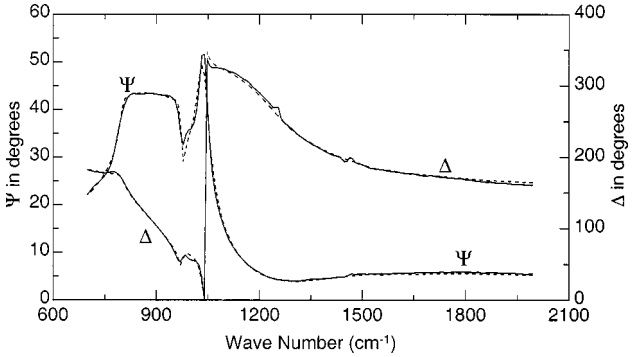


FIG. 14. Ellipsometric data and model spectra ($\Psi$ and $\Delta$), for H+ implanted sample (sample 10, $10^{16}$H+ $cm^{-2}$ implanted at 100 keV). Solid lines are experimental data and dashed lines are models.

also seen in electrical measurements and is sometimes called carrier spilling.[44]

The ellipsometric spectrum of sample 10, the $10^{16}\,cm^{-2}$ hydrogen-implanted substrate with a doping of approximately $9\times10^{18}\,N\,cm^{-3}$, looks remarkably similar to sample 8, the epilayer with similar substrate doping (see Figs. 3 and 14). That is, the optical response of the implanted layer is similar to an undoped epilayer. However, unlike the epilayer samples, the best fit is obtained only when the residual interband absorptions ($\varepsilon_{\infty\parallel,\perp}$) of the implanted layer is fit independently of substrate values. The best fit occurs when the parameter $\varepsilon_{\infty\perp}=6.2$ for the substrate and $\varepsilon_{\infty\perp}=6.6$ for the H-implanted layer. This increase in $\varepsilon_{\infty\perp}$, along with the deactivation in free-carrier concentrations in the H-implanted region, suggests that $H^+$ implantation into SiC at room temperature causes residual damage. Trap states that form in the gap capture the free electrons and thus reduce the free-carrier density. These conclusions are supported by Rutherford backscattering channeling experiments on similar samples.[45]

## VII. CONCLUSIONS

IR-SE in the 700–4000 $cm^{-1}$ spectral range is able to quantify free-electron concentrations $\geqslant10^{18}\,cm^{-3}$ in bulk and epitaxial SiC. Since the sensitivity is proportional to $\lambda^2$, lower concentrations could be detected by extending the spectral range into the far infrared. The technique can also quantitatively determine the thickness of the epitaxial layer, and is sensitive to the infrared-active one-phonon absorption at 800 $cm^{-1}$ and two-phonon summation bands between 1300 and 1700 $cm^{-1}$. The line shape near the LO-phonon energy region (960 to 1050 $cm^{-1}$) depends on phonon and effective mass anisotropy as well as phonon damping, carrier concentration, and the presence of a surface layer (via the Berreman effect).

Data from 6H-SiC can be modeled effectively only if we account for its large effective mass anisotropy (we used $m_\parallel^*=1.7$ and $m_\perp^*=0.25$). Effective mass anisotropy had no noticeable affect on the 4H-SiC spectra, which is known to have considerably less effective mass anisotropy than 6H-SiC (Ref. 37).

It is also useful to include the two-phonon interactions in the region from 1300 to 1700 $cm^{-1}$, because they influence the ellipsometric line shapes of that region. This in turn affects the calculation of the free-carrier concentration.

We have shown that IR-SE can be applied to quantitative, nondestructive, and contactless measurement of free carriers in SiC and other semiconductors. The technique is rapid and uses a commercial instrument. These measurements correlate well with low-frequency (dc) electrical measurements, and compliment SIMS and other techniques that quantify the concentration of dopant species. Previous work with dopant ion implant in silicon[7,8] has demonstrated that IR-SE can also determine graded free-carrier profiles. We have also shown that IR-SE can be applied to the study of phonon interactions and phonon and carrier anisotropies.

## ACKNOWLEDGMENTS

We are grateful to M. Schubert, P. Snyder, and I. Adhihetty for their stimulating discussions. This research was supported by NSF Grant No. DMI-9761473 and by the Center for Microelectronic and Optical Materials Research.

[1] A. Röseler, *Infrared Spectroscopic Ellipsometry* (Akademie-Verlag, Berlin, 1990).

[2] *Proceedings of the First International Conference on Spectroscopic Ellipsometry, Paris, France*, edited by A. C. Boccara, C. Pickering, and J. Rivory (Elsevier, Amsterdam, 1993), pp. 307–370; Thin Solid Films **234**, 307 (1993).

[3] *Proceedings of the Second International Conference on Spectroscopic Ellipsometry, Charlseton, South Carolina*, edited by R. W. Collins, D. E. Aspnes, and E. A. Irene (Elsevier, Amsterdam, 1998), pp. 625–741; Thin Solid Films **313-314**, 625 (1998).

[4] S. Ballon, E. Compain, and B. Drevillon, Rev. Sci. Instrum. **66**, 3269 (1995).

[5] J. Humlíček, R. Henn, and M. Cardona, Appl. Phys. Lett. **69**, 2581 (1996).

[6] J. Humlíček, Thin Solid Films **313-314**, 687 (1998).

[7] J. Humlíček, Phys. Status Solidi B **215**, 155 (1999).

[8] T. E. Tiwald, D. W. Thompson, and J. A. Woollam, J. Vac. Sci. Technol. B **16**, 312 (1998).

[9] T. E. Tiwald, D. W. Thompson, J. A. Woollam, W. Paulson, and R. Hance, Thin Solid Films **313-314**, 662 (1998).

[10] P. G. Snyder, T. E. Tiwald, D. W. Thompson, N. J. Ianno, J. A. Woollam, M. G. Mauk, and Z. A. Shellenbarger, Thin Solid Films **313–314**, 668 (1998).

[11] J. Humlíček and A. Röseler, Thin Solid Films **234**, 332 (1993).

[12] J. Humlíček, Philos. Mag. **70**, 699 (1994).

[13] D. W. Thompson, M. J. DeVries, T. E. Tiwald, and J. A. Woollam, Thin Solid Films **313-314**, 342 (1998).

[14] E. Franke, H. Neumann, M. Schubert, T. E. Tiwald, J. A. Woollam, and J. Hahn, Appl. Phys. Lett. **70**, 1668 (1997).

[15] W. G. Spitzer, D. Kleinman, and D. Walsh, Phys. Rev. **113**, 127 (1959).

[16] W.J. Choyke and L. Patrick, in *Silicon Carbide—1973*, edited by R. C. Marshall, J. W. Faust, Jr., C. E. Ryan (University of South Carolina Press, Columbia, SC, 1974), p. 261.

[17] W. J. Choyke and E. D. Palik, in *Handbook of Optical Constants of Solids*, edited by E. D. Palik (Academic, Orlando, 1985), pp. 587–595.
[18] F. Engelbrecht and R. Helbig, Phys. Rev. B **48**, 15 698 (1993).
[19] M. F. Macmillan, A. Henry, and E. Janzén, J. Electron. Mater. **27**, 300 (1998).
[20] R. M. A. Azzam and N. M. Bashara, *Ellipsometry and Polarized Light* (North-Holland, New York, 1977).
[21] M. Schubert, Phys. Rev. B **53**, 4265 (1996).
[22] L. Patrick and W. J. Choyke, Phys. Rev. **123**, 813 (1961).
[23] D. W. Berreman, Phys. Rev. **130**, 2193 (1963).
[24] P. Y. Yu and M. Cardona, *Fundamentals of Semiconductor Physics* (Springer, 1995, Berlin).
[25] R. T. Holm, J. W. Gibson, and E. D. Palik, J. Appl. Phys. **48**, 212 (1977).
[26] F. Bechstedt, P. Käckell, A. Zywietz, K. Karch, B. Adolph, K. Tenelsen, and J. Furthmüller, Phys. Status Solidi B **202**, 35 (1997).
[27] D. W. Feldman, J. H. Parker, W. J. Choyke, and L. Patrick, Phys. Rev. **173**, 787 (1968).
[28] J. Lekner, *Theory of Reflection* (Martinus Nijhoff, Dordrecht, 1987), pp. 142–143.
[29] I. G. Lang and U. S. Pasabekova, Fiz. Tverd. Tela. (Leningrad) **6**, 3640 (1965) [Sov. Phys. Solid State **6**, 2913 (1965)].
[30] M. Born and E. Wolf, *Principles of Optics*, 5th ed. (Pergamon, Oxford, 1975), p. 668.
[31] M. C. Simon and L. I. Perez, Optik (Stuttgart) **82**, 37 (1989).
[32] M. C. Simon and L. I. Perez, Optik (Stuttgart) **86**, 18 (1990).
[33] P. J. Colwell and M. V. Klein, Phys. Rev. B **6**, 498 (1972).
[34] R. P. Devaty and W. J. Choyke, Phys. Status Solidi A **162**, 5 (1997).
[35] S. Yoshida, in *Properties of Silicon Carbide*, edited by G. L. Harris (INSPEC, London, 1995), p. 69; G. L. Harris, H. S. Henry, and A. Jackson, *ibid.*, p. 63.
[36] N. T. Son, O. Kordina, A. O. Konstantinov, W. M. Chen, E. Sörman, B. Monemar, and E. Janzén, Appl. Phys. Lett. **65**, 3209 (1994).
[37] W. R. L. Lambrecht, S. Limpijumnong, and B. Segall, in IOP Conf. Proc. No. 142 (Institute of Physics, London, 1995), p. 263.
[38] N. T. Son, W. M. Chen, O. Kordina, A. O. Kosntantinov, B. Monemar, and E. Janzén, Appl. Phys. Lett. **66**, 1074 (1995).
[39] C. M. Herzinger, P. G. Snyder, B. Johs, and J. A. Woollam, J. Appl. Phys. **77**, 1715 (1995).
[40] R. Henn, C. Bernhard, A. Wittlin, M. Cardona, and S. Uchida, Thin Solid Films **313-314**, 642 (1998).
[41] C. Kittel, *Introduction to Solid State Physics* (Wiley, New York, 1996), pp. 287–294.
[42] S. Zollner, J. P. Carrejo, T. E. Tiwald, and J. A. Woollam, Phys. Status Solidi B **208**, R3 (1998).
[43] B. Harbecke, B. Heinz, B. Offermann, and W. Theiß, in *Optical Characterization of Epitaxial Semiconductor Layers*, edited by G. Bauer and W. Richter (Springer-Verlag, Berlin, 1996), p. 252.
[44] I. Czech, T. Clarysse, and W. Vandervorst, J. Vac. Sci. Technol. B **12**, 298 (1994).
[45] R. B. Gregory, T. A. Wetteroth, S. R. Wilson, O. W. Holland, and K. K. Thomas (unpublished).